Synergistic Effect of Chemical Substitution and Insertion on the Thermoelectric Performance of Cu26V2Ge6S32 Colusite

Yuta Shimizu, Koichiro Suekuni, Hikaru Saito, P. Lemoine, Emmanuel Guilmeau, Bernard Raveau, Raju Chetty, Michihiro Ohta, Toshiro Takabatake, Michitaka Ohtaki

Synergistic Effect of Chemical Substitution and Insertion on the Thermoelectric Performance of $Cu_{26}V_2Ge_6S_{32}$ Colusite

Yuta Shimizu, Koichiro Suekuni, Hikaru Saito, Pierric Lemoine, Emmanuel Guilmeau, Bernard Raveau, Raju Chetty, Michihiro Ohta, Toshiro Takabatake, Michitaka Ohtaki*

Y. Shimizu,
Interdisciplinary
Graduate School of Engineering Sciences, Kyushu University, Kasuga, Fukuoka 816-8580, Japan

Dr. K. Suekuni, Prof. M. Ohtaki
Interdisciplinary Graduate School of Engineering Sciences, Kyushu University, Kasuga, Fukuoka 816–8580, Japan
Transdisciplinary Research and Education Center for Green Technologies, Kyushu University, Kasuga, Fukuoka 816-8580, Japan
E-mail: suekuni.koichiro.063@m.kyushu-u.ac.jp

Dr. H. Saito
Institute for Materials Chemistry and Engineering, Kyushu University, Kasuga, Fukuoka 816-8580, Japan

Dr. P. Lemoine
Université de Rennes 1, CNRS, ISCR-UMR 6226, F-35000 Rennes, France

Dr. E. Guilmeau, Prof. B. Raveau
CRISMAT, CNRS, Normandie Université, ENSICAEN, UNICAEN, 14000 Caen, France

Dr. R. Chetty, Dr. M. Ohta
Global Zero Emission Research Center, National Institute of Advanced Industrial Science and Technology (AIST), Tsukuba, Ibaraki 305-8569, Japan

Prof. T. Takabatake
Graduate School of Advanced Science and Engineering, Hiroshima University, Higashi-Hiroshima 739-8530, Japan

Keywords: thermoelectric, sulfide, colusite, elemental substitution, interstitials, thermal conductivity

Abstract

Copper-based sulfides are promising materials for thermoelectric applications, which can convert waste heat into electricity. This study reports the enhanced thermoelectric performance of $Cu_{26}V_2Ge_6S_{32}$ colusite via substitution of antimony (Sb) for germanium (Ge) and introduction of copper (Cu) as an interstitial atom. The crystal structure of the solid solutions and Cu-rich compounds were analyzed by powder X-ray diffraction and scanning transmission electron microscopy. Both chemical approaches decrease the hole carrier concentration, which leads to a reduction in the electronic thermal conductivity while keeping the thermoelectric power factor at a high value. Furthermore, the interstitial Cu atoms act as phonon scatterers, thereby decreasing the lattice thermal conductivity. The combined effects increase the dimensionless thermoelectric figure of merit *ZT* from 0.3 ($Cu_{26}V_2Ge_6S_{32}$) to 0.8 ($Cu_{29}V_2Ge_5SbS_{32}$) at 673 K.

1. Introduction

Renewable energy sources, which include sunlight, heat, and vibration, play a crucial role in realizing a sustainable society. One of the promising applications for harvesting heat to generate electricity is the thermoelectric (TE) generator, which is composed of solid-state elements.[1–3] The conversion from thermal to electrical energy in solids is based on the Seebeck effect. The electronic potential difference (electromotive force) ΔV is generated in proportion to the temperature difference ΔT ($\Delta V = S\Delta T$, where S is the Seebeck coefficient) between two ends of an element. The electromotive force is utilized to supply electricity to an electronic device. Therefore, highly efficient TE conversion requires an element material to have large S. Other requisite characteristics of a TE material include low electrical resistivity ρ to reduce the internal resistance of the generator and low thermal conductivity κ to maintain sufficient ΔT. By combining these parameters (ρ, S, κ), the performance of a TE material can be determined using the expression: $ZT = S^2T\rho^{-1}\kappa^{-1}$, where ZT is referred to as the dimensionless figure of merit, T is the absolute temperature, and κ is the sum of its electronic component κ_{ele} and lattice component κ_{lat}. In addition to high performance (high ZT), natural-abundance and non-toxic characteristics are desired for TE materials used in large-scale applications. As such TE materials, Cu–S-based (degenerate) semiconductors have emerged in the recent decade.[4,5] Examples include Cu_2ZnSnS_4,[6] $CuFeS_2$,[7,8] $Cu_{1.8}S$,[9] Cu_2S,[10] $Cu_{12}Sb_4S_{13}$,[11–13] Cu_3SbS_4,[14] Cu_5FeS_4,[15–18] Cu_2SnS_3,[19] $Cu_4Sn_7S_{16}$,[20] $Cu_8Fe_3Sn_2S_{12}$,[21] $CuFe_2S_3$,[22] $Cu_{22}Fe_8Ge_4S_{32}$,[23] Cu_3PS_4,[24] and $Cu_{26}V_2Ge_6S_{32}$.[25,26] The last example is a synthetic member of the colusite family: $Cu_{26}T_2M_6S_{32}$ (T = Ti, V, Nb, Ta, Cr, Mo, W; M = Ge, Sn, Sb).[25–30] Colusites have attracted increasing attention due to their high ZT value ranging from 0.5–1.0 at 673 K.[26–43]

$Cu_{26}T_2M_6S_{32}$ colusites crystallize in a cubic structure ($P\bar{4}3n$), which is composed of three types of tetrahedral units: CuS_4, TS_4, and MS_4.[44,45] The CuS_4 and MS_4 tetrahedra share corners to construct a three-dimensional framework structure, which is completed by the TS_4

tetrahedra sharing edges with CuS_4 (Figure 1). The formal valence of the atoms can be represented as $Cu^{+}_{26}T^{4+}_{2}M^{5+}_{6}S^{2-}_{32}$ for T = Ti, $Cu^{+}_{22}Cu^{2+}_{4}T^{5+}_{2}M^{4+}_{6}S^{2-}_{32}$ for T = V, Nb, and Ta, $Cu^{+}_{24}Cu^{2+}_{2}T^{6+}_{2}M^{4+}_{6}S^{2-}_{32}$ for T = Cr, Mo, and W. The non-magnetic and *p*-type degenerate semiconducting characteristics of the colusites with T = V, Cr, Mo, and W were confirmed by TE and magnetic susceptibility measurements,[25] Mössbauer spectroscopy,[46] and first-principles electronic-structure calculations.[26,28,36] These characteristics indicate the itinerant nature of 3d holes of Cu^{2+}.[28,47] The calculations showed that the Fermi level (E_F) lies at the top of the valence band (VB), which primarily comprises the hybridized orbitals of Cu-3d and S-3p.[26,28,36] The nature of the VB indicates that the Cu–S-based tetrahedral framework governs the electronic properties. Depending on the compositions, a high power factor $S^2\rho^{-1}$ of 0.5–1.9 mW K^{-2} m^{-1} at 673 K can be achieved in colusites.[26–43] The tetrahedral framework also causes low $\kappa_{lat} \leq 1$ W K^{-1} m^{-1} due to its complexity and low-energy (~10 meV) optical phonon modes involving motions of Cu and S.[28,29,36] Further decrease in κ_{lat} can be achieved by introducing various types of defects into the crystal structure: interstitial defects, anti-site defects between cations, and splitted Cu site.[36,37,46] These defects are simultaneously produced by an excessive amount of sulfur sublimation upon heating above 973 K.[36,37]

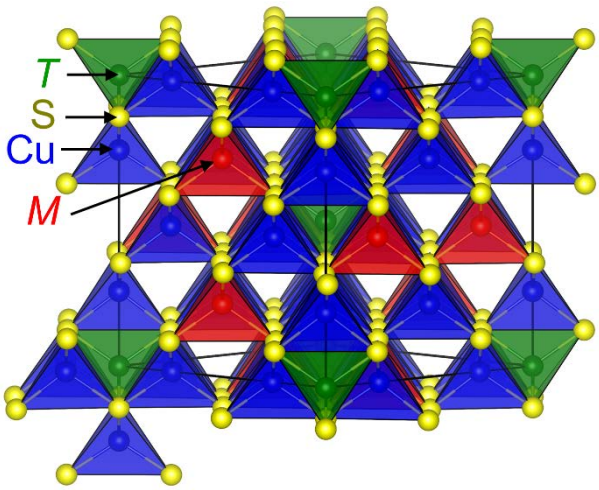

Figure 1. Crystal structure of $Cu_{26}T_2M_6S_{32}$ (T = Ti, V, Nb, Ta, Cr, Mo, W; M = Ge, Sn, Sb) colusite.

A good approach to introduce phonon scatterers (defects) into the colusite structure is by increasing the sintering temperature;[36, 37] however, the difficulty in controlling sulfur loss prevents fine-tuning of the hole carrier concentration *n*. Therefore, an alternative strategy to reduce κ_{lat} is required. Generally, substitutional doping of a heavier atom for a constituent atom results in a decrease in κ_{lat}.[48] Another possible way to reduce κ_{lat} in colusites is to introduce interstitial defects (atoms), according to the aforementioned results.[37] However, the effect of interstitial atoms on κ_{lat} has not been sorely examined for colusites to date. Following these circumstances, this study aimed to clarify the effects of substituting Sb for Ge and Cu insertion on κ_{lat} in $Cu_{26}V_2Ge_6S_{32}$ colusite. Hence, novel Sb-substituted ($Cu_{26}V_2Ge_{6-x}Sb_xS_{32}$), Cu-rich ($Cu_{26+y}V_2Ge_6S_{32}$), and combined Sb-substituted and Cu-rich ($Cu_{26+y}V_2Ge_{6-x}Sb_xS_{32}$ with $x = 1$) series were synthesized and their TE properties were investigated. Notably, these samples were sintered at 873 K, which is mandatory for limiting the sublimation of sulfur.[36,37,49]

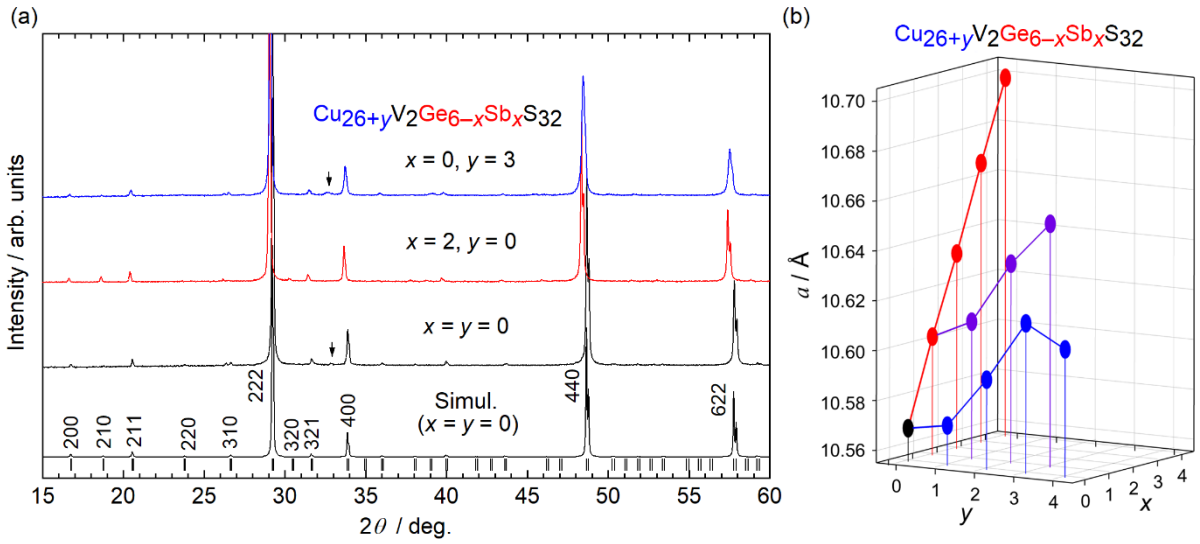

Figure 2. (a) Powder X-ray diffraction patterns and (b) lattice parameters *a* for $Cu_{26}V_2Ge_{6-x}Sb_xS_{32}$, $Cu_{26+y}V_2Ge_6S_{32}$, and $Cu_{26+y}V_2Ge_{6-x}Sb_xS_{32}$ (x = 1) samples. In (a), the diffraction patterns for $x = y = 0$, $x = 2$, $y = 0$ and $x = 0$, $y = 3$, and the simulated pattern based on the colusite ($Cu_{26}V_2Ge_6S_{32}$) structure are shown. Arrows for $x = y = 0$ and $x = 0$, $y = 3$ denote peaks from Cu_2S. The diffraction patterns for all samples are presented in Figures S1–S3.

2. Results and Discussion

The powder X-ray diffraction (PXRD) patterns of the samples in different series of compositions, *i.e.*, $Cu_{26}V_2Ge_{6-x}Sb_xS_{32}$ (x = 0–4), $Cu_{26+y}V_2Ge_6S_{32}$ (y = 0–4), and $Cu_{26+y}V_2Ge_{6-x}Sb_xS_{32}$ (x = 1, y = 0–3) are presented in Figure 2a and Figures S1–S3. For all samples, the positions and relative intensities of the diffraction peaks reasonably agree with that of a simulated pattern based on the colusite structure ($Cu_{26}V_2Ge_6S_{32}$, $P\bar{4}3n$). Note that the systematic presence of weak-intensity diffraction peaks (at 26.4° and 43.7° for x = 0) is originated from CuK_β radiation passing through a Ni filter. The diffraction patterns for $x = y = 0$ (pristine sample) and $y \geq 1$ (Cu-rich samples) exhibited small peaks from a secondary phase Cu_2S, and that for x = 4 (Sb-substituted sample) showed a small peak from an unidentified

phase (Figures S1–S3). For the Cu-rich series, the peak width became broader as *y* increased (Figures S2 and S3).

Rietveld refinement of the PXRD patterns of the Sb-substituted series ($Cu_{26}V_2Ge_{6-x}Sb_xS_{32}$) (Figure S4–S8 and Table S1), leading to low-reliability factors, confirmed the validity of the structural model of colusites, which includes seven crystallographic sites: three for Cu (6*d*, 8*e*, 12*f*), one for V (2*a*), one for Ge/Sb (6*c*) and two for S (8*e*, 24*i*). The lattice parameter *a* linearly increased from 10.5684(2) Å for $x = 0$ by 1.2% as *x* increased to 4, as shown in Figure 2b and Table S1. The lattice expansion can be attributed to the larger ionic radius of Sb^{5+} (0.565 Å)[50] than that for Ge^{4+} (0.390 Å).[51] In fact, the occupation factor of Sb at Ge (6*c*) site obtained from Rietveld refinement increased with *x* and reached 62% (*i.e.* $Cu_{26}V_2Ge_{2.3}Sb_{3.7}S_{32}$) for $x = 4$ (Table S1). The increase in the Sb content was also clearly observed from the evolution of $h + k + l = 2n + 1$ peaks (*e.g.* 210, 320, see Figure 2a and Figure S1)[29]. It was further confirmed that this substitution increases the *M*(6*c*)–S(24*i*) (*M* = Ge, Sb) distance from 2.254 Å for $x = 0$ to 2.383 Å for $x = 4$ while keeping the average Cu–S distance intact (2.291–2.300 Å) (Table S1). This indicates the limited modification of Cu–S-based tetrahedral framework. It should be noted that the presence of Sb^{5+} in tetrahedral coordination of sulfides was only reported for famatinite Cu_3SbS_4[52] and the colusite sister compound $Cu_{26}Ti_2Sb_6S_{32}$.[29]

For the Cu-rich series ($Cu_{26+y}V_2Ge_6S_{32}$ and $Cu_{26+y}V_2Ge_{6-x}Sb_xS_{32}$ with $x = 1$), Rietveld refinement of the PXRD patterns confirmed a lattice expansion attributed to Cu insertion (Figure 2b). More specifically, *a* increased slightly for $y = 1$ and increased by 0.44% and 0.47% for $y = 3$ in $Cu_{26+y}V_2Ge_6S_{32}$ and $Cu_{26+y}V_2Ge_{6-x}Sb_xS_{32}$ ($x = 1$), respectively. Saturation of the *a* value for $Cu_{30}V_2Ge_6S_{32}$ ($y = 4$) suggests a lower (actual) Cu content, which is consistent with the increase in the amount of the Cu-rich secondary phase (Cu_2S) for $y = 4$ and reflects a limit of Cu insertion into the VGe-colusite structure. A possible mechanism of the lattice expansion for the Cu-rich series deals with the introduction of Cu atoms into

interstitial sites, as previously reported for $Cu_{26}Nb_2Sn_6S_{32-\delta}$ colusite.[37] The fact that Cu insertion leads to electron doping (decrease in *n*), as shown below, strongly supports this mechanism.

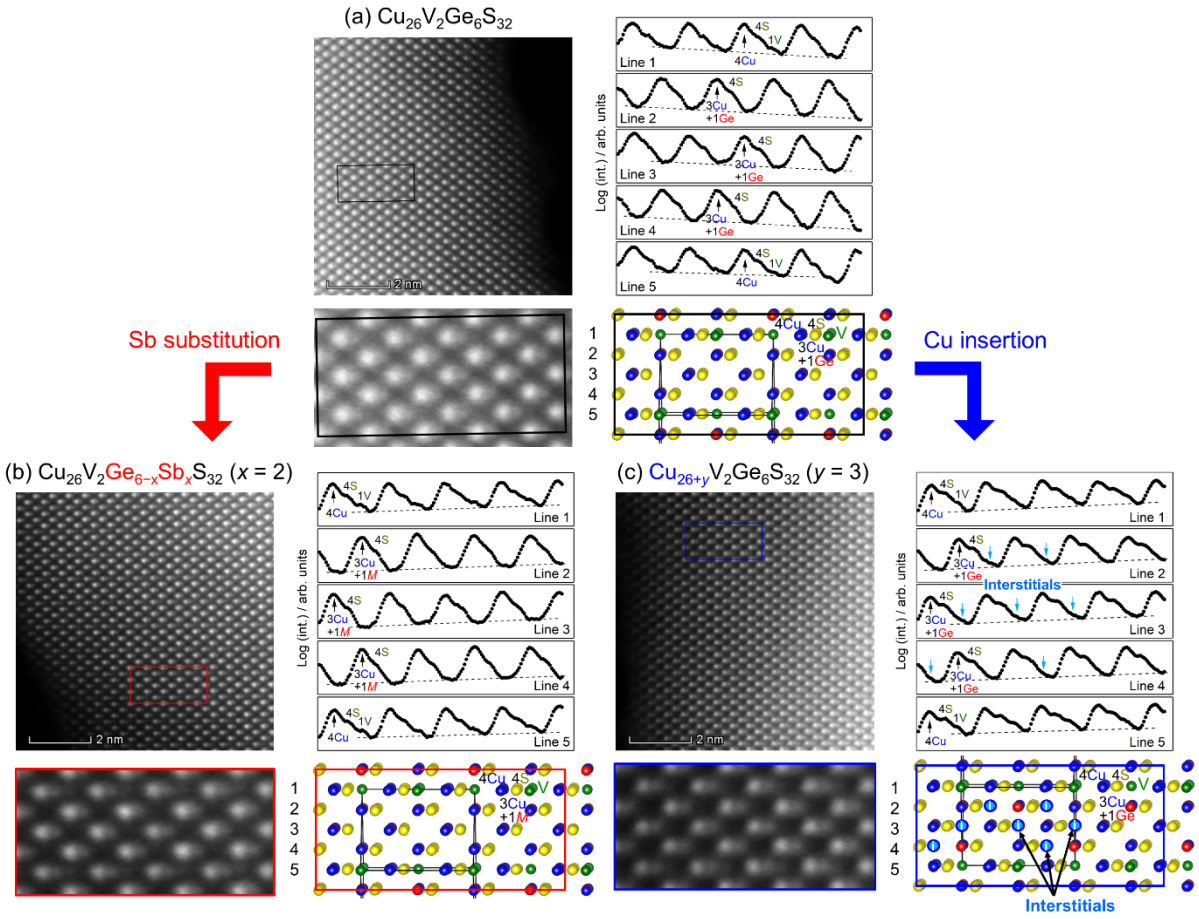

Figure 3. Annular dark-field scanning transmission electron microscopy (STEM) images for (a) $Cu_{26}V_2Ge_6S_{32}$, (b) $Cu_{26}V_2Ge_{6-x}Sb_xS_{32}$ (x = 2), and (c) $Cu_{26+y}V_2Ge_6S_{32}$ (y = 3) samples along the [110] directions. Expanded views of the STEM images and the corresponding views of the colusite structure are also shown. The bright spots in the annular dark-field STEM images show atomic columns. Along this direction, there are four types of columns labelled "4Cu", "1V", "3Cu+*M*" / "3Cu+Ge", and "4S" (see text). Here, the numeral denotes the number of atoms periodically contained in the columns, and *M* means "(4Ge + 2Sb) / 6". Logarithmic intensities (levels of brightness) of columns along "lines" denoted by 1–5 in the expanded views are plotted in the graphs. The dashed lines in the graphs are eye guides for

making peaks/humps clear. For (b) $Cu_{26+y}V_2Ge_6S_{32}$ (y = 3), the intensity along a line composed of the "3Cu + 1Ge" and "4S" columns shows a hump at an interstitial position. Such a hump was hardly noticed for (a) $Cu_{26}V_2Ge_6S_{32}$ and (c) $Cu_{26}V_2Ge_{6-x}Sb_xS_{32}$ (x = 2).

To confirm the existence of interstitial Cu ions, scanning transmission electron microscopy (STEM) analysis was performed for pristine, Sb-substituted, and Cu-rich samples, as shown in Figure 3 and Figures S9–S12. The annular dark-field (ADF) STEM images for $Cu_{26}V_2Ge_6S_{32}$, $Cu_{26}V_2Ge_{6-x}Sb_xS_{32}$ with x = 2, and $Cu_{26+y}V_2Ge_6S_{32}$ with y = 3 showed well-aligned atom columns with intensities (levels of brightness in the image) that are mostly consistent with those expected from the pristine colusite ($Cu_{26}V_2Ge_6S_{32}$) structure. Along the [110] direction (Figure 3), there were four types of columns: pure copper columns labelled "4Cu", pure vanadium columns labelled "1V", pure sulfur columns labelled "4S", and mixed columns containing besides copper either mixtures of Ge and Sb labelled "3Cu + 1*M*" or only Ge labelled "3Cu + 1Ge". Here, the numeral denotes the number of atoms periodically contained in the columns and *M* means "(4Ge + 2Sb) / 6". Bearing in mind that the intensity of the spots corresponding to the columns is approximately proportional to the square of the atomic number *Z* (29 for Cu, 32 for Ge, 51 for Sb, 23 for V and 16 for S), one can expect a decrease in their relative intensity from "3Cu + 1*M*" to "3Cu + 1Ge" to "4Cu" to "4S" to "1V" columns and that the intensities of the "3Cu + 1Ge" and "4Cu" columns are comparable. As a result, the "3Cu + 1*M*" / "3Cu + 1Ge", "4Cu" and "4S" columns are clearly identified in the STEM images. As shown in the line profiles of the intensity (Figure 3 and Figures S10 and S12), the relative intensities of the "3Cu + 1*M*" column were higher than that of the "3Cu + 1Ge" column, which is consistent with the substitution of Sb for Ge determined from PXRD analyses. The line profile also allows us to see the "1V" columns, whose position agrees with that of the colusite structure.

Remarkably, for the Cu-rich sample ($Cu_{26+y}V_2Ge_6S_{32}$ with y = 3), the logarithmic intensity along the line composed of "3Cu + 1Ge" and "4S" columns showed a hump at an interstitial position for the colusite structure (Figure 3c). Such a hump was hardly noticed in the pristine and Sb-substituted samples, $Cu_{26}V_2Ge_6S_{32}$ and $Cu_{26}V_2Ge_{6-x}Sb_xS_{32}$ with x = 2 (Figures 3a, 3b). These results strongly indicate the existence of atoms at interstitial sites in the Cu-rich sample. This position may be consistent with the presence of Cu at an interstitial 24*i* site (0.255, 0.215, 0.032), as determined by the powder synchrotron X-ray diffraction for $Cu_{26}Nb_2Sn_6S_{32-\delta}$.[37] However, signals from interstitial atoms were observed at a part of "columns" of the interstitial sites. This suggests a non-uniform arrangement (or aggregation) of interstitial atoms, which might result in the broadening of diffraction peaks (Figure 2a and Figure S2). Signals from interstitial ions in the STEM images along the [100] and [111] directions (Figures S9–S12) could not be extracted. These results reflect a preferential direction, [110], for the aggregation of interstitial atoms and/or might be due to very weak contribution to the intensity from the interstitial atoms compared with the other ones.

The existence of interstitial atoms was further confirmed by Rietveld refinement of the PXRD pattern for $Cu_{26+y}V_2Ge_6S_{32}$ with y = 3 (Figure S13). Refinement based on the colusite structure showed a residual electron density at an interstitial 24*i* site (0.236, 0.235, 0.007). Then, refinement based on a colusite structure with interstitial Cu atom at the 24*i* site (atomic coordinates being fixed) was performed, which significantly improved the reliability factors (Table S2). The refined occupation factor at the 24*i* site was 0.042(1), which corresponds to an extra 1.0 Cu atom per formula unit, *i.e.* $Cu_{27}V_2Ge_6S_{32}$. Although the quality of the PXRD pattern was not sufficient for quantitative analysis (*e.g.* broadened peaks), the refinement confirmed partial occupation of a 24*i* site (~0.24, ~0.24, ~0.01) by extra atoms.

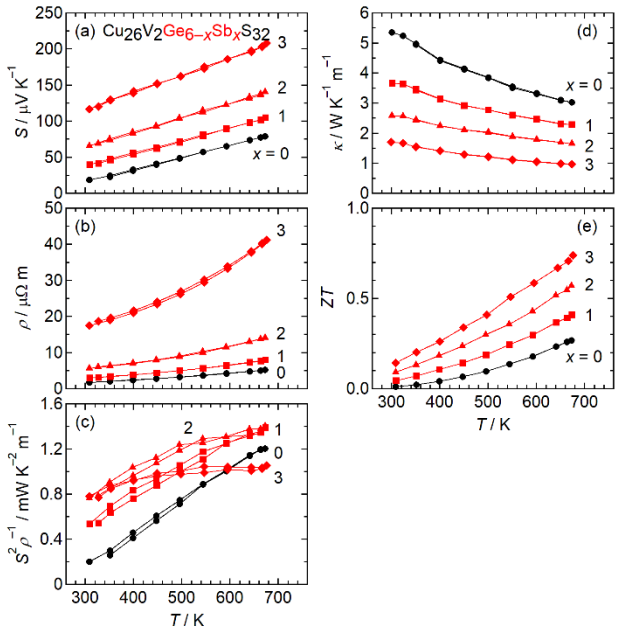

Figure 4. (a) Seebeck coefficient S, (b) electrical resistivity ρ, (c) power factor $S^2\rho^{-1}$, (d) thermal conductivity κ and (e) dimensionless figure of merit ZT for $Cu_{26}V_2Ge_{6-x}Sb_xS_{32}$ samples.

Next, the TE properties for the three series of samples were discussed (except for x = 4 and y = 4). All samples had relative densities higher than 95%, as confirmed by scanning electron microscopy (SEM) (Figure S14). For the Sb-substituted series ($Cu_{26}V_2Ge_{6-x}Sb_xS_{32}$), all samples exhibited the *p*-type metallic behavior of degenerated semiconductors. The pristine sample (x = 0) had low S (18 μV K^{-1}) and ρ (1.7 μΩ m) values at 300 K (Figures 4a and 4b), which is in agreement with previous studies.[25,28] The values of S and ρ increase with x and reaches 116 μV K^{-1} and 17 μΩ m, respectively, for x = 3. The increase in S and ρ results from a decrease in n from 6.8×10^{21} cm^{-3} for x = 0 to 1.9×10^{21} cm^{-3} for x = 3 (*i.e.* electron doping) (Table S3), which can be attributed to the larger valence of Sb^{5+} compared to Ge^{4+}. As a result, the power factor $S^2\rho^{-1}$ increased from 1.2 mW K^{-2} m^{-1} for x = 0 to 1.4 mW K^{-2} m^{-1} for x = 1 and x = 2, and then decreased to 1.0 mW K^{-2} m^{-1} for x = 3 at 673 K (Figure 4c). The increase in ρ led to a strong reduction in κ_{ele}, that manifested itself in the form of a drastic

decrease in κ (Figure 4d). Consequently, the combination of enhanced $S^2\rho^{-1}$ and reduced κ resulted in the enhancement of ZT from 0.3 (x = 0) to 0.7 (x = 3) at 673 K for the Sb-substituted samples (Figure 4e).

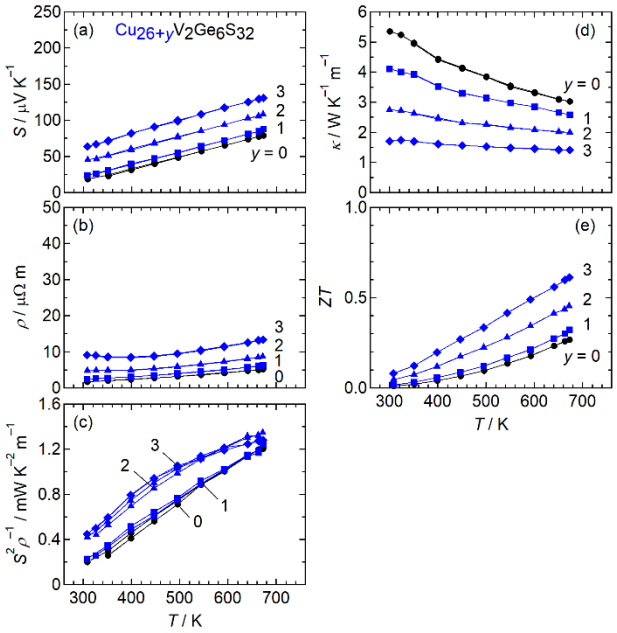

Figure 5. (a) Seebeck coefficient S, (b) electrical resistivity ρ, (c) power factor $S^2\rho^{-1}$, (d) thermal conductivity κ and (e) dimensionless figure of merit ZT for $Cu_{26+y}V_2Ge_6S_{32}$ samples.

For the Cu-rich series ($Cu_{26+y}V_2Ge_6S_{32}$), the values of S and ρ increased with y (Figures 5a and 5b), and it is consistent with a decrease in n from 6.8×10^{21} cm^{-3} for y = 0 to 4.1×10^{21} cm^{-3} for y = 3 at 300 K (Table S3). The decrease in n originates from that the insertion of Cu^+ doped electron into the VB. As a result, $S^2\rho^{-1}$ remains at a high level (1.2–1.4 mW K^{-2} m^{-1}) at 673 K (Figure 5c). The value of κ decreases with y due to the reduction in κ_{ele} (Figure 5d). Consequently, ZT values increase from 0.3 (y = 0) to 0.6 (y = 3) at 673 K (Figure 5e).

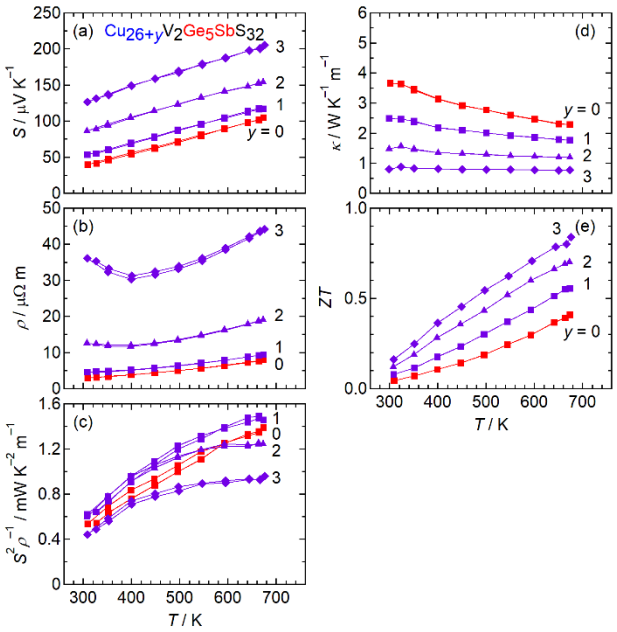

Figure 6. (a) Seebeck coefficient S, (b) electrical resistivity ρ, (c) power factor $S^2\rho^{-1}$, (d) thermal conductivity κ and (e) dimensionless figure of merit ZT for $Cu_{26+y}V_2Ge_{6-x}Sb_xS_{32}$ (x = 1) samples.

For the combined Sb-substituted and Cu-rich series ($Cu_{26+y}V_2Ge_{6-x}Sb_xS_{32}$ with x = 1), the increase in S and ρ (Figure 6a and 6b) with increasing y is consistent with the aforementioned results for $Cu_{26+y}V_2Ge_6S_{32}$ (Figure 5a and 5b). Remarkably, an increase in ρ was observed at temperatures below 400 K for $Cu_{26+y}V_2Ge_{6-x}Sb_xS_{32}$ (x = 1, y =3) (Figure 6b), unlike the metallic behaviour observed in ρ for $Cu_{26}V_2Ge_{6-x}Sb_xS_{32}$ (x = 3) (Figure 4b). Because the samples of x = 1, y = 3 and x = 3 have similar n at 300 K (*i.e.*, 1.7×10^{21} cm^{-3} for x =1, y = 3; 1.9×10^{21} cm^{-3} for x = 3), the enlargement of ρ for x =1, y = 3 can be attributed to a decrease in the electron mobility μ_H from 1.9 cm^2 V^{-1} s^{-1} to 1.0 cm^2 V^{-1} s^{-1} (Table S3). Also, because the electronic properties of colusite are governed by the Cu–S tetrahedral framework,[39] the presence of interstitial atoms probably affects μ_H in the conductive network. A similar upturn in ρ was observed in cation-rich $[Cu_{26}Cr_2Ge_6]_{1+\delta}S_{32}$ colusites.[40] As a result of the aforementioned variation of y for $Cu_{26+y}V_2Ge_{6-x}Sb_xS_{32}$ (x = 1), the value of $S^2\rho^{-1}$ at 300

K remains unchanged, whereas it increases at 673 K for $y = 1$ and decreases for $y \geq 2$ (Figure 6c). The sample produced at $x = 1$, $y = 1$ showed the highest $S^2\rho^{-1}$ value of 1.5 mW K^{-2} m^{-1} at 673 K compared to the other samples in this study. The value of κ (and κ_{ele}) decreased as y increased (Figure 6d). As a result, the reduction in κ boosts ZT at 673 K from 0.4 ($x = 1$, $y = 0$) to 0.8 ($x = 1$, $y = 3$) (Figure 6e). The ZT value of the samples produced at $x = 1$, $y = 3$ in the $Cu_{26+y}V_2Ge_{6-x}Sb_xS_{32}$ series was higher than that of $x = 3$ in the $Cu_{26}V_2Ge_{6-x}Sb_xS_{32}$ series (Figure 4e) despite similar values of S and ρ at 673 K (Figures 4 and 6). This comparison indicates that the reduction in κ_{lat} via Cu insertion contributes to the enhancement of ZT.

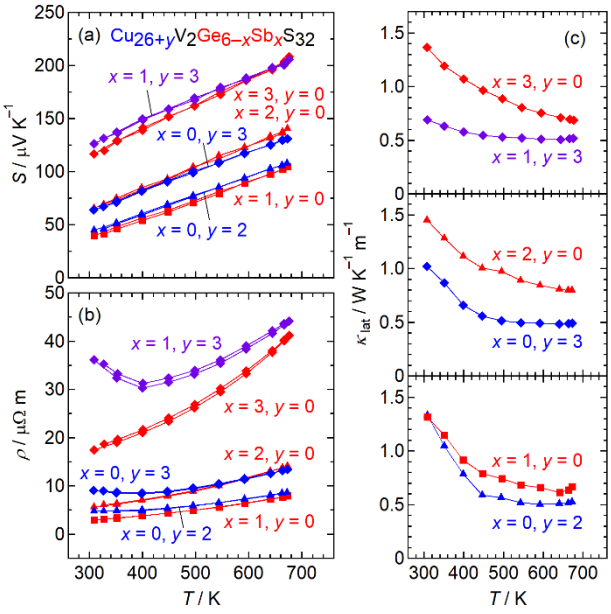

Figure 7. (a) Seebeck coefficient S, (b) electrical resistivity ρ and (c) lattice thermal conductivity κ_{lat} for the selected $Cu_{26+y}V_2Ge_{6-x}Sb_xS_{32}$ samples (see text).

To determine the effects of Sb substitution and Cu insertion on κ_{lat}, the value of κ_{lat} was estimated by subtracting $\kappa_{ele} = LT\rho^{-1}$ from κ, where $L = 1.5 + \exp(-|S|/116)$.[53] The equation regarding L is based on the acoustic phonon scattering of electrons, which is consistent with the metallic increase in $\rho(T)$ at temperatures between 400 K and 673 K for all the samples (Figures 4b, 5b, and 6b). Conversely, single parabolic band assumed for the

equation may be too simple to describe the VB of colusites. As shown in Figure S15, the obtained κ_{lat} for $Cu_{26}V_2Ge_{6-x}Sb_xS_{32}$, $Cu_{26+y}V_2Ge_6S_{32}$, and $Cu_{26+y}V_2Ge_{6-x}Sb_xS_{32}$ (x = 1) exhibited complicated variations with different x and y values. More specifically, κ_{lat} for $Cu_{26}V_2Ge_{6-x}Sb_xS_{32}$ increased for x = 2 and decreased for x = 3. For the $Cu_{26+y}V_2Ge_6S_{32}$ series, κ_{lat} slightly increased for $y \geq 1$, whereas for the $Cu_{26+y}V_2Ge_{6-x}Sb_xS_{32}$ (x = 1) series, κ_{lat} decreased for $y \geq 1$. These opposite trends for the Cu-rich series imply that the variation of κ_{lat} is not influenced by the existence of Cu_2S (secondary phase), whose amount increased with y in both series. The variations of κ_{lat} can originate from different effects/mechanisms: (i) the substitutional doping of Sb for Ge, (ii) the interstitial doping of Cu, (iii) uncertainty in the estimation of L, due to the complexity of the actual electronic structure[28] and (iv) phonon scattering by electrons.[54] Hence, we chose three pairs of samples in the $Cu_{26+y}V_2Ge_{6-x}Sb_xS_{32}$ series with similar S and ρ values (equivalent n and E_F) to minimise the influence of (iii) and (iv) on κ. Each pair includes Sb-substituted/non-Cu-rich and Cu-rich samples (*i.e.* x = 1, y = 0 ($n = 5.5 \times 10^{21}$ cm^{-3} at 300 K) vs. x = 0, y = 2 (5.1×10^{21} cm^{-3}); x = 2, y = 0 (4.0×10^{21} cm^{-3}) vs. x = 0, y = 3 (4.1×10^{21} cm^{-3}); x = 3, y = 0 (1.9×10^{21} cm^{-3}) vs. x = 1, y = 3 (1.7×10^{21} cm^{-3})). As shown in Figure 7, although the substitution of Sb for Ge has a negligible effect on κ_{lat}, all Cu-rich samples showed lower κ_{lat} compared with the non-Cu-rich samples. This result demonstrates that the interstitial Cu ions act as phonon scatterers in the crystal structure, leading to the reduction of κ_{lat}. Furthermore, the decrease in κ_{lat} at approximately 300 K was more pronounced in the samples showing larger upturn in $\rho(T)$. This means that the insertion of Cu has a significant impact on both enhanced phonon scattering and reduced μ_H (Table S3). Further investigations (*e.g.*, Mössbauer spectroscopy, extended X-ray absorption fine structure spectroscopy) are required to investigate the local structure modification of the colusite structure.

3. Conclusion

In this work, we performed the substitution of Sb for Ge and the insertion of Cu into the crystal structure of $Cu_{26+y}V_2Ge_{6-x}Sb_xS_{32}$ colusite. Both chemical approaches led to a decrease in n and κ_{ele}, while maintaining $S^2\rho^{-1} \geq 0.9$ mW K^{-2} m^{-1} (at $x \leq 3$, $y \leq 3$). Furthermore, the interstitial Cu atoms act as phonon scatterers, leading to the suppression of κ_{lat}. These combined effects boost ZT, which reaches a value of 0.8 at 673 K for $x = 1$, $y = 3$ sample. Thus, the Cu insertion into corner sharing three-dimensional tetrahedral framework structures of Cu–S-based materials is a powerful chemical approach for improving TE performance via tuning of n and reducing of κ_{lat}.

4. Experimental Section

The samples of $Cu_{26}V_2Ge_{6-x}Sb_xS_{32}$ (x = 0–3), $Cu_{26+y}V_2Ge_6S_{32}$ (y = 0–4) and $Cu_{26+y}V_2Ge_{6-x}Sb_xS_{32}$ (x = 1, y = 0–3) were prepared by directly reacting the constituent elements at 1373 K followed by heat treatment at 873 K as reported for the samples of $Cu_{26}Nb_2Sn_6S_{32}$.[37] The obtained samples were pulverized using a planetary ball mill (Pulverisette 7 premium line, Fritsch) operating at room temperature at a disk rotation speed of 450 rpm for 1 h. The sample powder was put into a jar together with seven balls of 10 mm diameter in an Ar atmosphere. The jar and balls were made of tungsten carbide (WC). The pulverized sample was loaded into a WC die with an inner diameter of 10 mm. The sample was sintered at 823/873 K for 40 min in a flowing N_2 atmosphere under a uniaxial pressure of 200 MPa in a hot-press sintering furnace (PLASMAN CSP-I-03121, S. S. Alloy). The relative density of the samples was higher than 95% of the theoretical density. The sintered sample was cut and polished into bars and discs to measure the TE properties.

PXRD data were collected in the range of 10° ≤ 2θ ≤ 100° using an X-ray diffractometer (MiniFlex600, RIGAKU) with a Cu K_α radiation source. PXRD data analyzes

were performed by Rietveld refinement using the FullProf and WinPlotr software packages.[55, 56] Zero-point shift, lattice parameter, peak shape parameters, asymmetry parameters, fractional atomic coordinates and isotropic displacement parameters were refined after manually removing the background contribution. The density of the sample was checked by SEM using a microscope (JCM-6000Plus NeoScope, JEOL). Atomic-resolution observations were performed using a transmission electron microscope (Titan Cubed 60–300 G2, Thermo Fisher Scientific) which is equipped with a spherical aberration corrector (DCOR, CEOS) for the probe-forming lens system. The microscope was operated in the STEM mode at an accelerating voltage of 300 kV. The convergence semi-angle of the electron probe was set to 18 mrad. The typical probe diameter was less than 0.1 nm. An ADF detector was positioned to detect scattered electrons with an angular range from 38 to 184 mrad. Each sintered bulk sample was crushed and dispersed to ethanol in Ar atmosphere to avoid oxidation. Then, it was dropped on a carbon supporting film and was immediately inserted in the electron microscope.

S and ρ were simultaneously measured at T between 300 K and 673 K in a measurement system (ZEM-3, ADVANCE RIKO) in a helium atmosphere. Thermal diffusivity α and specific heat C_P at 300–673 K were measured simultaneously in a measurement system (LFA 457 MicroFlash, Netzsch) using the laser-flash method in a flowing Ar atmosphere. In this study, the sample was coated with a thin layer of graphite. The absolute values of C_P were derived from the comparison between the measured values and C_P values measured for a standard sample of Pyroceram 9606 (Netzsch) (Figure S16). These data were used to calculate κ as $\alpha C_P d_s$, where d_s represented sample density estimated from the dimensions and weight of the sample. Note that the obtained C_p values reasonably agreed among samples, which is comparable to the Dulong-Petit value at 300 K and higher by ≤ 16% at 673 K (Figure S16). The Hall-effect measurements were performed using a four-probe DC method on a laboratory-built system, with a permanent magnet generating a magnetic field of

0.62 T at 300 K. We calculated n as $R_H^{-1}e^{-1}$ and μ_H as $R_H\rho^{-1}$, based on the single-carrier model, where R_H is the Hall coefficient and e is the elementary charge.

Supporting Information

Supporting Information is available from the Wiley Online Library or from the author.

Acknowledgements

The authors would like to thank Enago (www.enago.jp) for the English language review. This work was financially supported by JSPS KAKENHI Grant No. JP20H02440 (K. S.), and grants from the International Joint Research Program for Innovative Energy Technology funded by METI and Research and Development Program for Promoting Innovative Clean Energy Technologies Through International Collaboration funded by NEDO. E.G. and P.L. acknowledge the financial support of CNRS through the International Emerging Actions program (EXPRESS project).

References

[1] L. E. Bell, *Science* **2008**, *321*, 1457.

[2] R. Freer, A. V. Powell, *J. Mater. Chem. C* **2020**, *8*, 441.

[3] M. A. Zoui, S. Bentouba, J. G. Stocholm, M. Bourouis, *Energies* **2020**, *13*, 3606.

[4] K. Suekuni, T. Takabatake, *APL Mater.* **2016**, *4*, 104503.

[5] A. V. Powell, *J. Appl. Phys.* **2019**, *126*, 100901.

[6] M. L. Liu, F. Q. Huang, L. D. Chen, I. W. Chen, *Appl. Phys. Lett.* **2009**, *94*, 202103.

[7] N. Tsujii, T. Mori, *Appl. Phys. Express* **2013**, *6*, 043001.

[8] H. Xie, X. Su, X. Zhang, S. Hao, T. P. Bailey, C. C. Stoumpos, A. P. Douvalis, X. Hu, C. Wolverton, V. P. Dravid, C. Uher, X. Tang, M. G. Kanatzidis, *J. Am. Chem. Soc.* **2019**, *141*, 18900.

[9] Z. H. Ge, B. P. Zhang, Y. X. Chen, Z. X. Yu, Y. Liu, J. F. Li, *Chem. Commun.* **2011**, *47*, 12697.

[10] Y. He, T. Day, T. Zhang, H. Liu, X. Shi, L. Chen, G. J. Snyder, *Adv. Mater.* **2014**, *26*, 3974.

[11] K. Suekuni, K. Tsuruta, T. Ariga, M. Koyano, *Appl. Phys. Express* **2012**, *5*, 051201.

[12] X. Lu, D. T. Morelli, Y. Xia, F. Zhou, V. Ozolins, H. Chi, X. Zhou, C. Uher, *Adv. Energy Mater.* **2013**, *3*, 342.

[13] K. Suekuni, K. Tsuruta, M. Kunii, H. Nishiate, E. Nishibori, S. Maki, M. Ohta, A. Yamamoto, M. Koyano, *J. Appl. Phys.* **2013**, *113*, 043712.

[14] K. Chen, B. Du, N. Bonini, C. Weber, H. Yan, M. J. Reece, *J. Phys. Chem. C* **2016**, *120*, 27135.

[15] P. Qiu, T. Zhang, Y. Qiu, X. Shi, L. Chen, *Energy Environ. Sci.* **2014**, *7*, 4000.

[16] G. Guélou, A. V. Powell, P. Vaqueiro, *J. Mater. Chem. C* **2015**, *3*, 10624.

[17] V. Pavan Kumar, T. Barbier, P. Lemoine, B. Raveau, V. Nassif, E. Guilmeau, *Dalton Trans.* **2017**, *46*, 2174.

[18] S. O. J. Long, A. V. Powell, P. Vaqueiro, S. Hull, *Chem. Mater.* **2018**, *30*, 456.

[19] Y. Shen, C. Li, R. Huang, R. Tian, Y. Ye, L. Pan, K. Koumoto, R. Zhang, C. Wan, Y. Wang, *Sci. Rep.* **2016**, *6*, 32501.

[20] C. Bourgès, P. Lemoine, O.I. Lebedev, R. Daou, V. Hardy, B. Malaman, E. Guilmeau, *Acta Mater.* **2015**, *97*, 180.

[21] V. Pavan Kumar, T. Barbier, V. Caignaert, B. Raveau, R. Daou, B. Malaman, G. L. Caër, P. Lemoine, E. Guilmeau, *J. Phys. Chem. C* **2017**, *121*, 16454.

[22] T. Barbier, D. Berthebaud, R. Frésard, O.I. Lebedev, E. Guilmeau, V. Eyerta, A. Maignan, *Inorg. Chem. Front.* **2017**, *4*, 424.

[23] V. Pavan Kumar, L. Paradis-Fortin, P. Lemoine, V. Caignaert, B. Raveau, B. Malaman, G. L. Caër, S. Cordier, E. Guilmeau, *Inorg. Chem.* **2017**, *56*, 13376.

[24] T. Tanimoto, K. Suekuni, T. Tanishita, H. Usui, T. Tadano, T. Kamei, H. Saito, H. Nishiate, C. H. Lee, K. Kuroki, M. Ohtaki, *Adv. Funct. Mater.* **2020**, 30, 2000973.

[25] K. Suekuni, F. S. Kim, T. Takabatake, *J. Appl. Phys.* **2014**, *116*, 063706.

[26] K. Suekuni, F. S. Kim, H. Nishiate, M. Ohta, H. I. Tanaka, T. Takabatake, *Appl. Phys. Lett.* **2014**, *105*, 132107.

[27] Y. Kikuchi, Y. Bouyrie, M. Ohta, K. Suekuni, M. Aihara, T. Takabatake, *J. Mater. Chem. A* **2016**, *4*, 15207.

[28] V. Pavan Kumar, A. R. Supka, P. Lemoine, O. I. Lebedev, B. Raveau, K. Suekuni, V. Nassif, R. Al Rahal Al Orabi, M. Fornari, E. Guilmeau, *Adv. Energy Mater.* **2019**, *9*, 1803249.

[29] T. Hagiwara, K. Suekuni, P. Lemoine, A. R. Supka, R. Chetty, E. Guilmeau, B. Raveau, M. Fornari, Michihiro Ohta, R. Al Rahal Al Orabi, H. Saito, K. Hashikuni, Michitaka Ohtaki, *Chem. Mater.* **2021**, in print.

[30] G. Guélou, P. Lemoine, B. Raveau, E. Guilmeau, *J. Mater. Chem. C* **2021**, *9*, 773.

[31] F. S. Kim, K. Suekuni, H. Nishiate, M. Ohta, H. I. Tanaka, T. Takabatake, *J. Appl. Phys.* **2016**, *119*, 175105.

[32] Y. Bouyrie, V. Ohorodniichuk, S. Sassi, P. Masschelein, A. Dauscher, C. Candolfi, B. Lenoir, *J. Electron. Mater.* **2017**, *46*, 2684.

[33] C. Bourgès, M. Gilmas, P. Lemoine, N. E. Mordvinova, O. I. Lebedev, E. Hug, V. Nassif, B. Malaman, R. Daoua, E. Guilmeau, *J. Mater. Chem. C* **2016**, *4*, 7455.

[34] Y. Bouyrie, M. Ohta, K. Suekuni, Y. Kikuchi, P. Jood, A. Yamamoto, T. Takabatake, *J. Mater. Chem. C* **2017**, *5*, 4174.

[35] Y. Bouyrie, M. Ohta, K. Suekuni, P. Jood, T. Takabatake, *J. Alloys Compd.* **2018**, *735*, 1838.

[36] C. Bourgès, Y. Bouyrie, A. R. Supka, R. Al Rahal Al Orabi, P. Lemoine, O. I. Lebedev, M. Ohta, K. Suekuni, V. Nassif, V. Hardy, R. Daou, Y. Miyazaki, M. Fornari E. Guilmeau, *J. Am. Chem. Soc.* **2018**, *140*, 2186.

[37] K. Suekuni, Y. Shimizu, E. Nishibori, H. Kasai, H. Saito, D. Yoshimoto, K. Hashikuni, Y. Bouyrie, R. Chetty, M. Ohta, E. Guilmeau, T. Takabatake, K. Watanabe, M. Ohtaki, *J. Mater. Chem. A* **2019**, *7*, 228.

[38] R. Chetty, Y. Kikuchi, Y. Bouyrie, P. Jood, A. Yamamoto, K. Suekuni, M. Ohta, *J. Mater. Chem. C* **2019**, *7*, 5184.

[39] V. Pavan Kumar, G. Guélou, P. Lemoine, B. Raveau, A. R. Supka, R. Al Rahal Al Orabi, M. Fornari, K. Suekuni, E. Guilmeau, *Angew. Chem. Int. Ed.* **2019**, *58*, 15455.

[40] G. Guélou, V. Pavan Kumar, A. Bourhim, P. Lemoine, B. Raveau, A. Supka, O. I. Lebedev, R. Al Rahal Al Orabi, M. Fornari, K. Suekuni, E. Guilmeau, *ACS Appl. Energy Mater.* **2020**, *3*, 4180.

[41] Y. Bouyrie, R. Chetty, K. Suekuni, N. Saitou, P. Jood, N. Yoshizawa, T. Takabatake, M. Ohta, *J. Mater. Chem. C* **2020**, *8*, 6442.

[42] G. Guélou, C. Couder, A. Bourhim, O. I. Lebedev, N. Daneu, F. Appert, J. Juraszek, P. Lemoine, L. Segreto, E. Guilmeau, *Acta Mater.* **2020**, *195*, 229.

[43] V. Pavan Kumar, S. Mitra, G. Guélou, A. R. Supka, P. Lemoine, B. Raveau, R. Al Rahal Al Orabi, M. Fornari, K. Suekuni, E. Guilmeau, *Appl. Phys. Lett.* **2020**, *117*, 173902.

[44] P. G. Spry, S. Merlino, S. Wang, X. Zhang, P. R. Buseck, *Am. Mineral.* **1994**, *79*, 750.

[45] O. V. Frank-Kamenetskaya, I. V. Rozhdestvenskaya, L. A. Yanulova, *J. Struct. Chem.* **2002**, *43*, 89.

[46] C. Candolfi, G. Guélou, C. Bourgès, A. R. Supka, R. Al Rahal Al Orabi, M. Fornari, B. Malaman, G. L. Caër, P. Lemoine, V. Hardy, J. M. Zanotti, R. Chetty, M. Ohta, K. Suekuni, E. Guilmeau, *Phys. Rev. Materials* **2020**, *4*, 025404.

[47] B. Raveau, *J. Supercond. Nov. Magn.* **2020**, *33*, 259.

[48] R. Gurunathan, R. Hanus, G. J. Snyder, *Mater. Horiz.* **2020**, *7*, 1452.

[49] P. Lemoine, V. Pavan Kumar, G. Guélou, V. Nassif, B. Raveau, E. Guilmeau, *Chem. Mater.* **2020**, *32*, 830.

[50] K. Chen, C. D. Paola, B. Du, R. Zhang, S. Laricchia, N. Bonini, C. Weber, I. Abrahams, H. Yan, M. Reece, *J. Mater. Chem. C* **2018**, *6*, 8546.

[51] R. D. Shannon, *Acta Crystallogr.* **1976**, *A32*, 751.

[52] J. Garin, E. Parthé, *Acta Cryst.* **1972**, *B28*, 3672.

[53] H. S. Kim, Z. M. Gibbs, Y. Tang, H. Wang, G. J. Snyder, *APL Mater.* **2015**, *3*, 041506.

[54] Q. Xu, J. Zhou, T. H. Liu, G. Chen, *Appl. Phys. Lett.* **2019**, *115*, 023903.

[55] J. Rodríguez-Carvajal, *Physica B Condens. Matter* **1993**, *192*, 55.

[56] T. Roisnel, J. Rodríguez-Carvajal, *Mater. Sci. Forum* **2001**, *378–381*, 118.

The table of contents entry should be 50–60 words long and should be written in the present tense and impersonal style (*i.e.* avoid we). The text should be different from the abstract text.

Y. Shimizu, K. Suekuni*, H. Saito, P. Lemoine, E. Guilmeau, B. Raveau, R. Chetty, M. Ohta, T. Takabatake, M. Ohtaki

Synergistic Effect of Chemical Substitution and Insertion on the Thermoelectric Performance of $Cu_{26}V_2Ge_6S_{32}$ Colusite

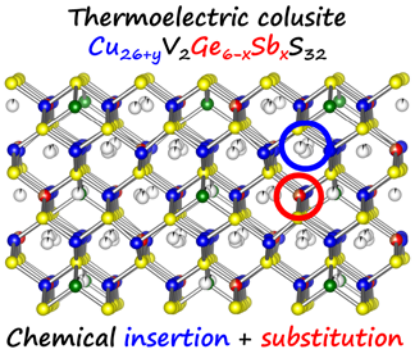

Supporting Information

Synergistic Effect of Chemical Substitution and Insertion on the Thermoelectric Performance of $Cu_{26}V_2Ge_6S_{32}$ Colusite

Yuta Shimizu, Koichiro Suekuni, Hikaru Saito, Pierric Lemoine, Emmanuel Guilmeau, Bernard Raveau, Raju Chetty, Michihiro Ohta, Toshiro Takabatake, Michitaka Ohtaki*

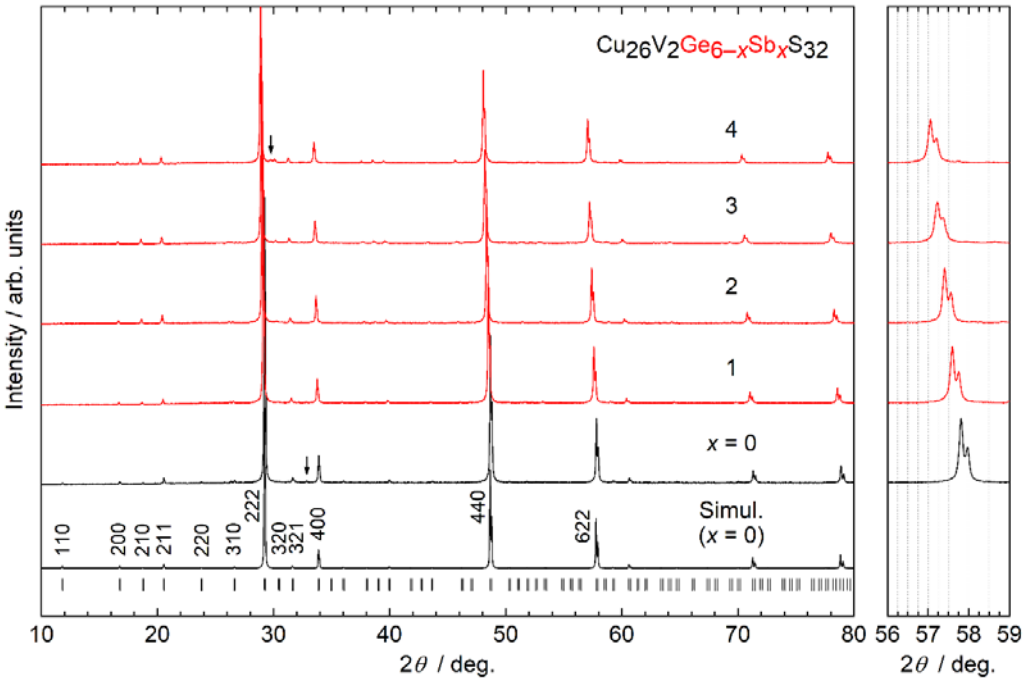

Figure S1. Powder X-ray diffraction patterns for $Cu_{26}V_2Ge_{6-x}Sb_xS_{32}$ samples. Arrows for x = 0 and x = 4 denote peaks from Cu_2S and an unidentified phase, respectively. The simulated pattern based on the colusite ($Cu_{26}V_2Ge_6S_{32}$) structure is shown at the bottom. The right panel shows expanded views of 622 peaks.

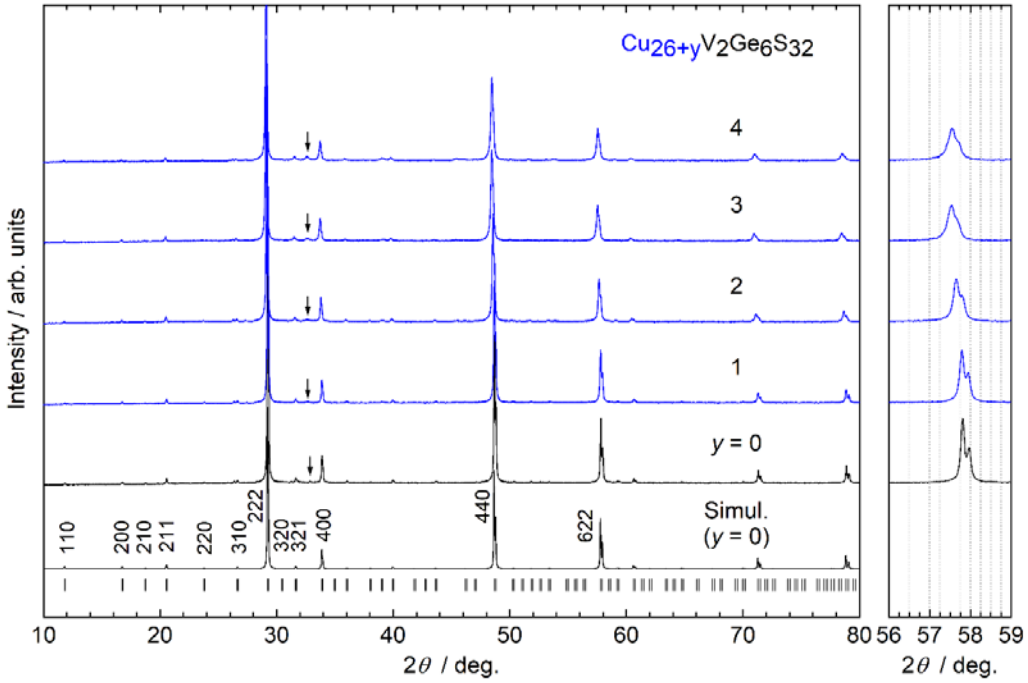

Figure S2. Powder X-ray diffraction patterns for $Cu_{26+y}V_2Ge_6S_{32}$ samples. Arrows denote peaks from Cu_2S. The simulated pattern based on the colusite ($Cu_{26}V_2Ge_6S_{32}$) structure is shown at the bottom. The right panel shows expanded views of 622 peaks.

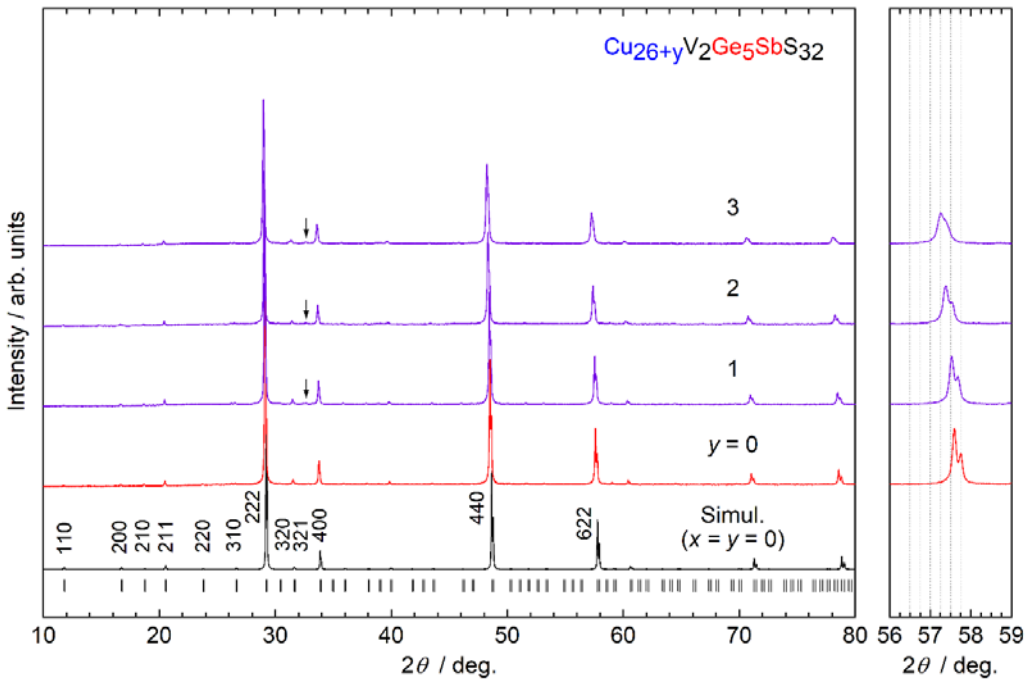

Figure S3. Powder X-ray diffraction patterns for $Cu_{26+y}V_2Ge_{6-x}Sb_xS_{32}$ (x = 1) samples. Arrows denote peaks from Cu_2S. The simulated pattern based on the colusite ($Cu_{26}V_2Ge_6S_{32}$) structure is shown at the bottom. The right panel shows expanded views of 622 peaks.

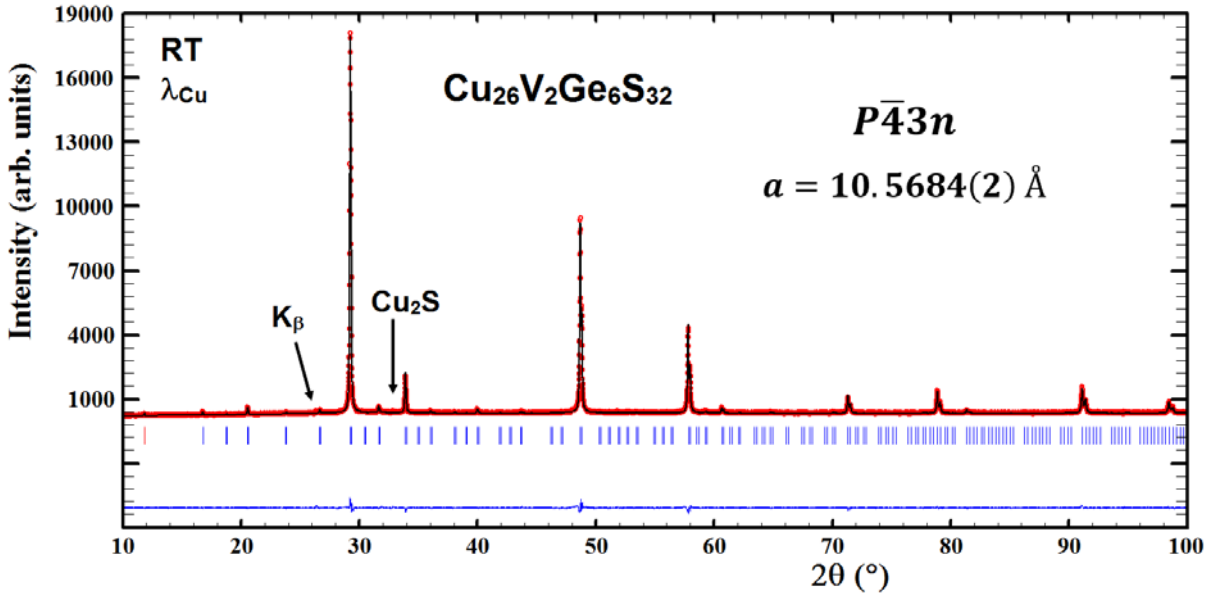

Figure S4. Rietveld refinement of power X-ray diffraction patterns for $Cu_{26}V_2Ge_6S_{32}$.

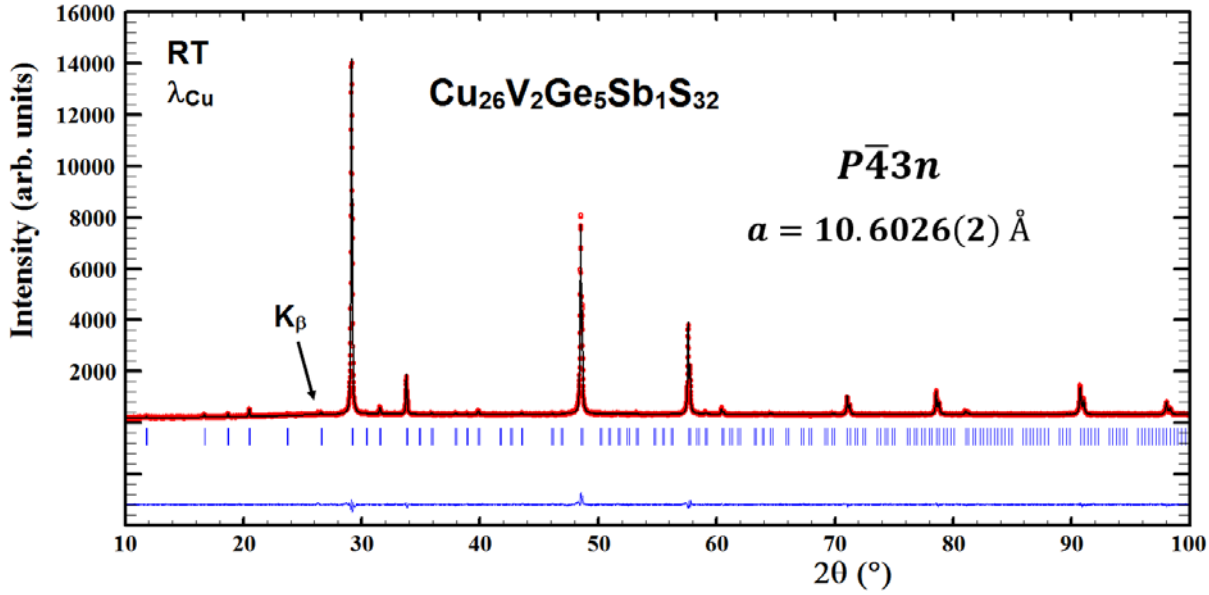

Figure S5. Rietveld refinement of power X-ray diffraction patterns for $Cu_{26}V_2Ge_{6-x}Sb_xS_{32}$ with $x = 1$.

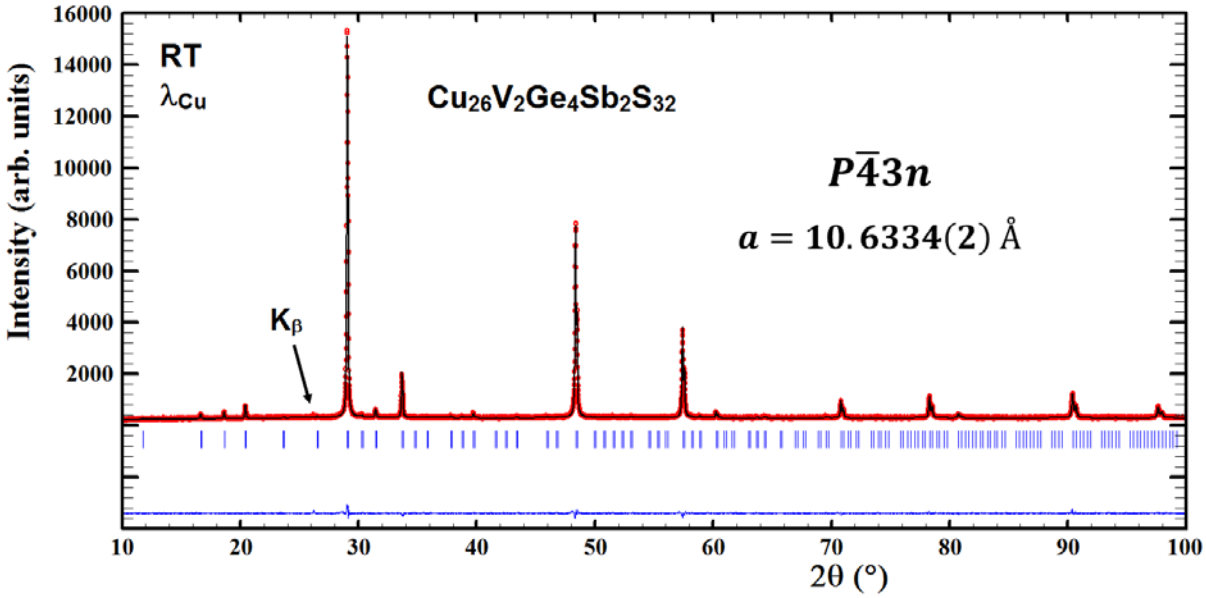

Figure S6. Rietveld refinement of power X-ray diffraction patterns for $Cu_{26}V_2Ge_{6-x}Sb_xS_{32}$ with $x = 2$.

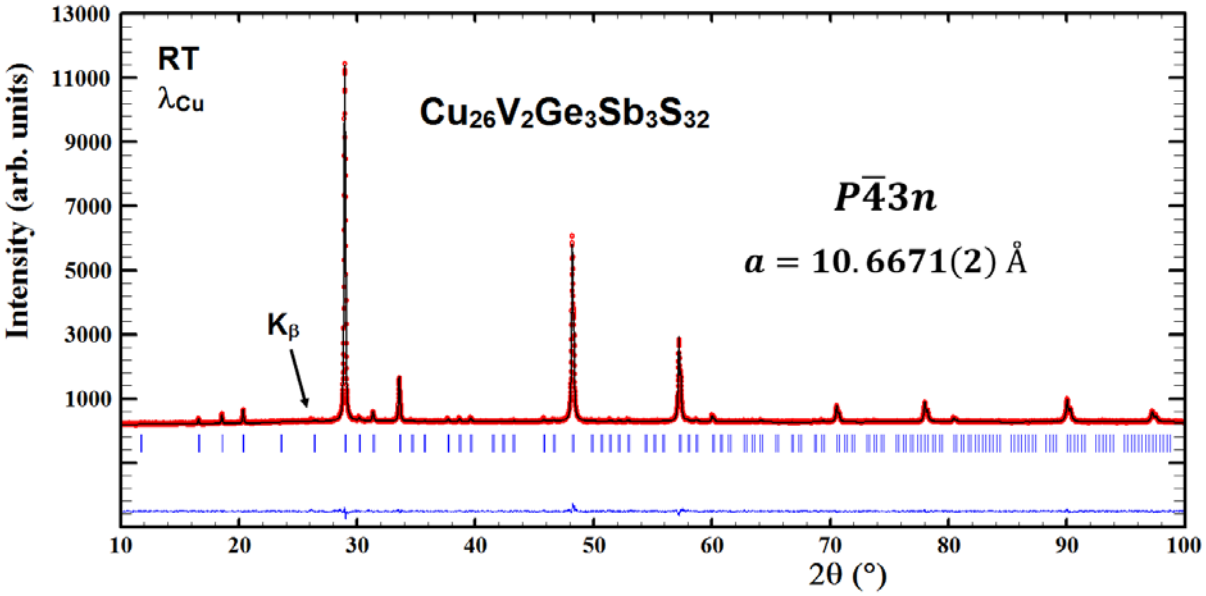

Figure S7. Rietveld refinement of power X-ray diffraction patterns for $Cu_{26}V_2Ge_{6-x}Sb_xS_{32}$ with $x = 3$.

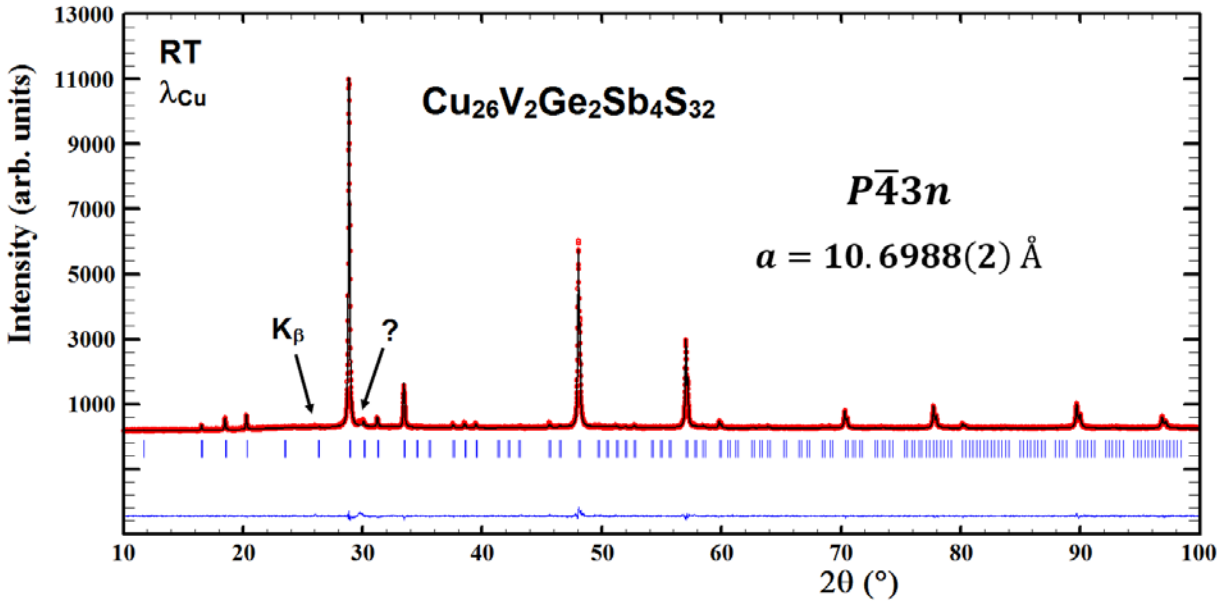

Figure S8. Rietveld refinement of power X-ray diffraction patterns for $Cu_{26}V_2Ge_{6-x}Sb_xS_{32}$ with $x = 4$.

Table S1. Results from the Rietveld refinements of power X-ray diffraction patterns for $Cu_{26}V_2Ge_{6-x}Sb_xS_{32}$ samples (space group $P\bar{4}3n$).

$Cu_{26}V_2Ge_{6-x}Sb_xS_{32}$	$x = 0$	$x = 1$	$x = 2$	$x = 3$	$x = 4$
a (Å)	10.5684(2)	10.6026(2)	10.6334(2)	10.6671(2)	10.6988(2)
SOF_Ge(6*c*)	1.00	0.87(2)	0.69(2)	0.50(2)	0.38(2)
SOF_Sb(6*c*)	-	0.13(2)	0.31(2)	0.50(2)	0.62(2)
*x*_Cu(8*e*)	0.248(1)	0.248(1)	0.247(1)	0.245(1)	0.246(1)
*x*_Cu(12*f*)	0.260(1)	0.260(1)	0.257(1)	0.257(1)	0.256(1)
*x*_S(8*e*)	0.126(1)	0.127(1)	0.125(1)	0.123(1)	0.124(1)
*x*_S(24*i*)	0.371(1)	0.371(1)	0.372(1)	0.375(1)	0.376(1)
*y*_S(24*i*)	0.373(1)	0.373(1)	0.372(1)	0.370(1)	0.368(1)
*z*_S(24*i*)	0.121(1)	0.122(1)	0.122(1)	0.126(1)	0.128(1)
χ^2	0.678	0.641	0.575	0.560	0.680
R_{wp} ; R_{exp}	4.09 ; 4.96	4.19 ; 5.23	3.98 ; 5.25	4.11 ; 5.49	4.62 ; 5.60
R_{Bragg} ; R_F	2.62 ; 7.54	3.05 ; 6.45	2.20 ; 5.37	2.72 ; 5.17	3.03 ; 6.29
Distances (Å)					
V(2*a*)-S(8*e*) × 4	2.308	2.325	2.297	2.267	2.296
V(2*a*)-Cu(12*f*) × 6	2.751	2.755	2.735	2.741	2.740
M(6*c*)-S(24*i*) × 4	2.254	2.269	2.291	2.349	2.383
Cu(6*d*)-S(24*i*) × 4	2.276	2.291	2.281	2.286	2.286
Cu(8*e*)-S(8*e*) × 1	2.237	2.220	2.245	2.265	2.255
Cu(8*e*)-S(24*i*) × 3	2.286	2.289	2.303	2.297	2.293
Cu(12*f*)-S(8*e*) × 2	2.359	2.366	2.346	2.341	2.348
Cu(12*f*)-S(24*i*) × 2	2.287	2.291	2.313	2.297	2.300
Cu-S (average)	2.291	2.297	2.300	2.298	2.298

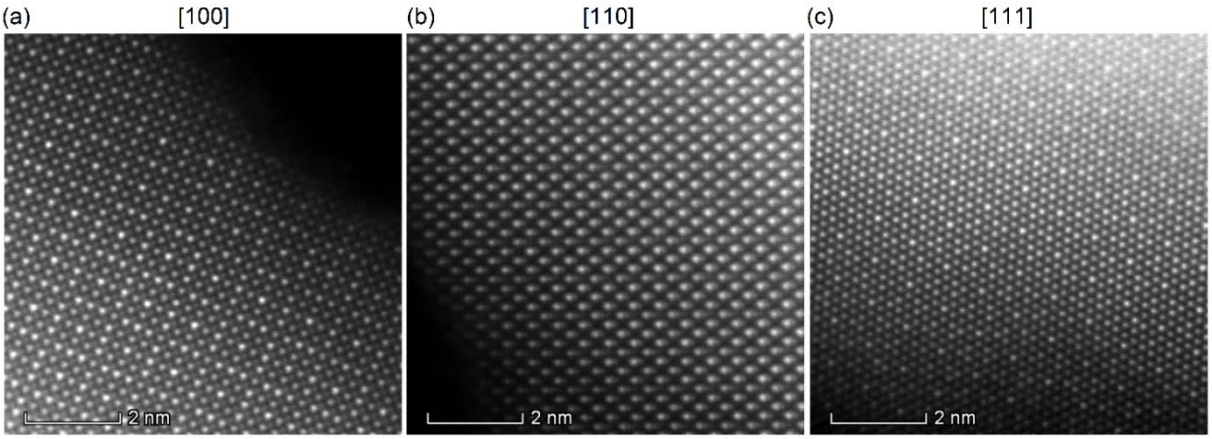

Figure S9. Annular dark-field scanning transmission electron microscopy images along the (a) 100, (b) 110 and (c) 111 directions for $Cu_{26}V_2Ge_{6-x}Sb_xS_{32}$ (x = 2) sample.

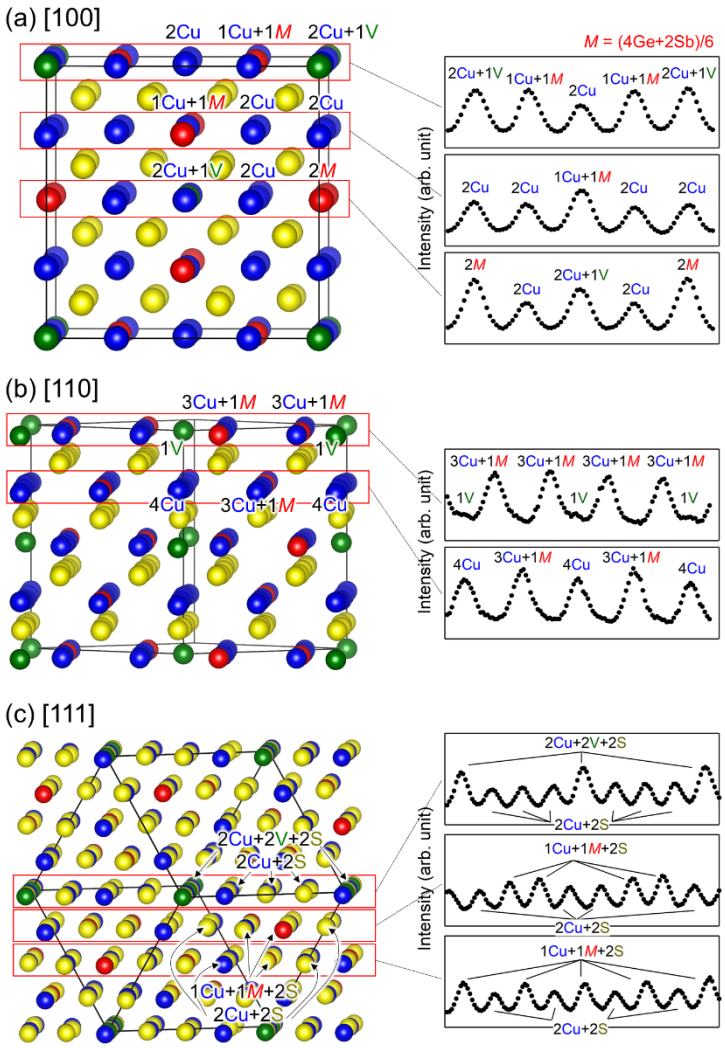

Figure S10. Line profiles of intensity for atomic columns along the (a) 100, (b) 110 and (c) 111 directions depicted in Figure S9 and the corresponding view of the crystal structure.

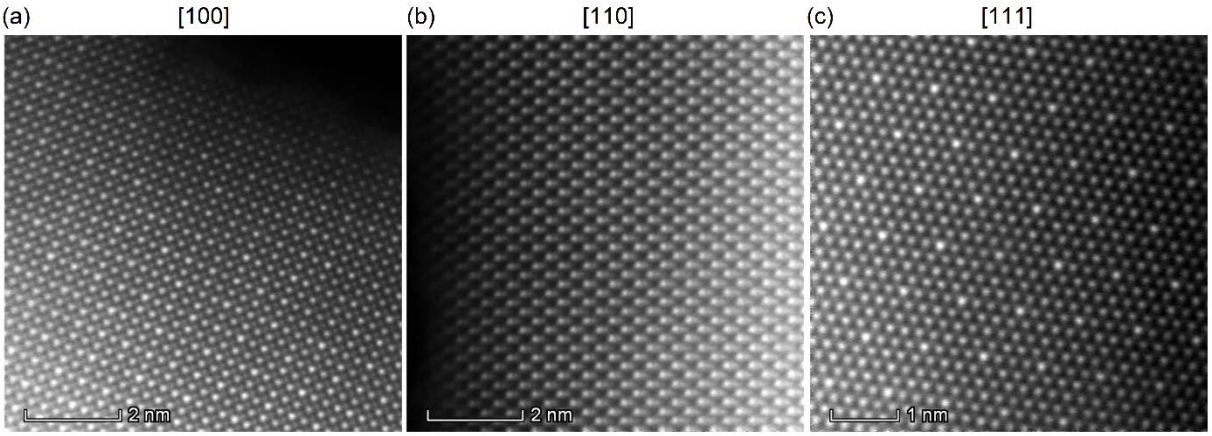

Figure S11. Annular dark-field scanning transmission electron microscopy images along the (a) 100, (b) 110 and (c) 111 directions for $Cu_{26+y}V_2Ge_6S_{32}$ (y = 3) sample.

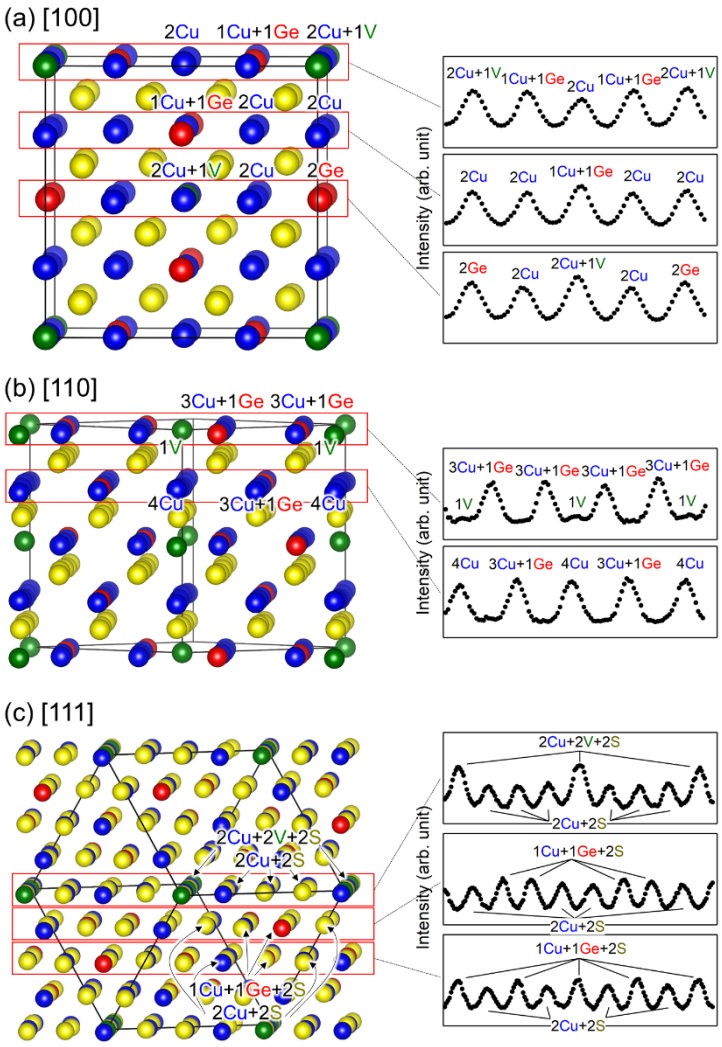

Figure S12. Line profiles of intensity for atomic columns along the (a) 100, (b) 110 and (c) 111 directions depicted in Figure S11 and the corresponding view of the crystal structure.

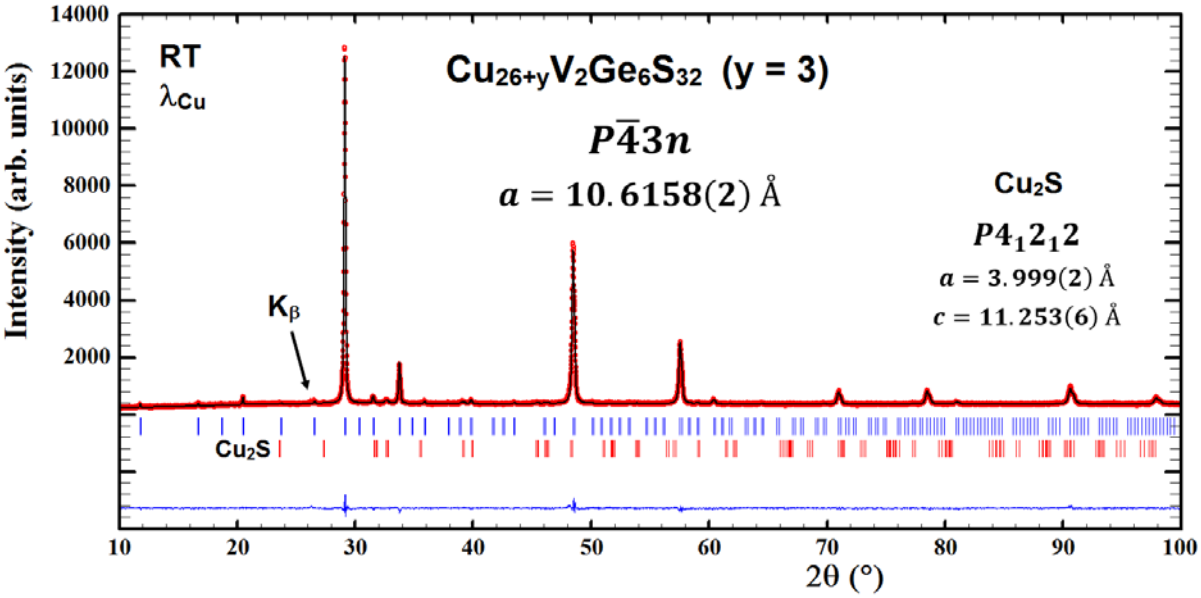

Figure S13. Rietveld refinement of power X-ray diffraction patterns for $Cu_{26+y}V_2Ge_6S_{32}$ with y = 3.

Table S2. Results from Rietveld refinements of powder X-ray diffraction patterns for y = 0 and y = 3 samples of $Cu_{26+y}V_2Ge_6S_{32}$ (space group $P\bar{4}3n$).

$Cu_{26+y}V_2Ge_6S_{32}$	y = 0	y = 3	y = 3
a (Å)	10.5684(2)	10.6149(2)	10.6158(2)
SOF_Cu(24*i*)*	—	—	0.042(1)
x_Cu(8*e*)	0.248(1)	0.247(1)	0.246(1)
x_Cu(12*f*)	0.260(1)	0.260(1)	0.260(1)
x_S(8*e*)	0.126(1)	0.127(1)	0.127(1)
x_S(24*i*)	0.371(1)	0.372(1)	0.372(1)
y_S(24*i*)	0.373(1)	0.372(1)	0.373(1)
z_S(24*i*)	0.121(1)	0.121(1)	0.120(1)
χ^2	0.678	0.760	0.651
R_{wp} ; R_{exp}	4.09 ; 4.96	4.21 ; 4.82	3.88 ; 4.81
R_{Bragg} ; R_F	2.62 ; 7.54	7.21 ; 10.5	4.11 ; 9.01

* Cu atoms in interstitial position (0.236, 0.235, 0.007)

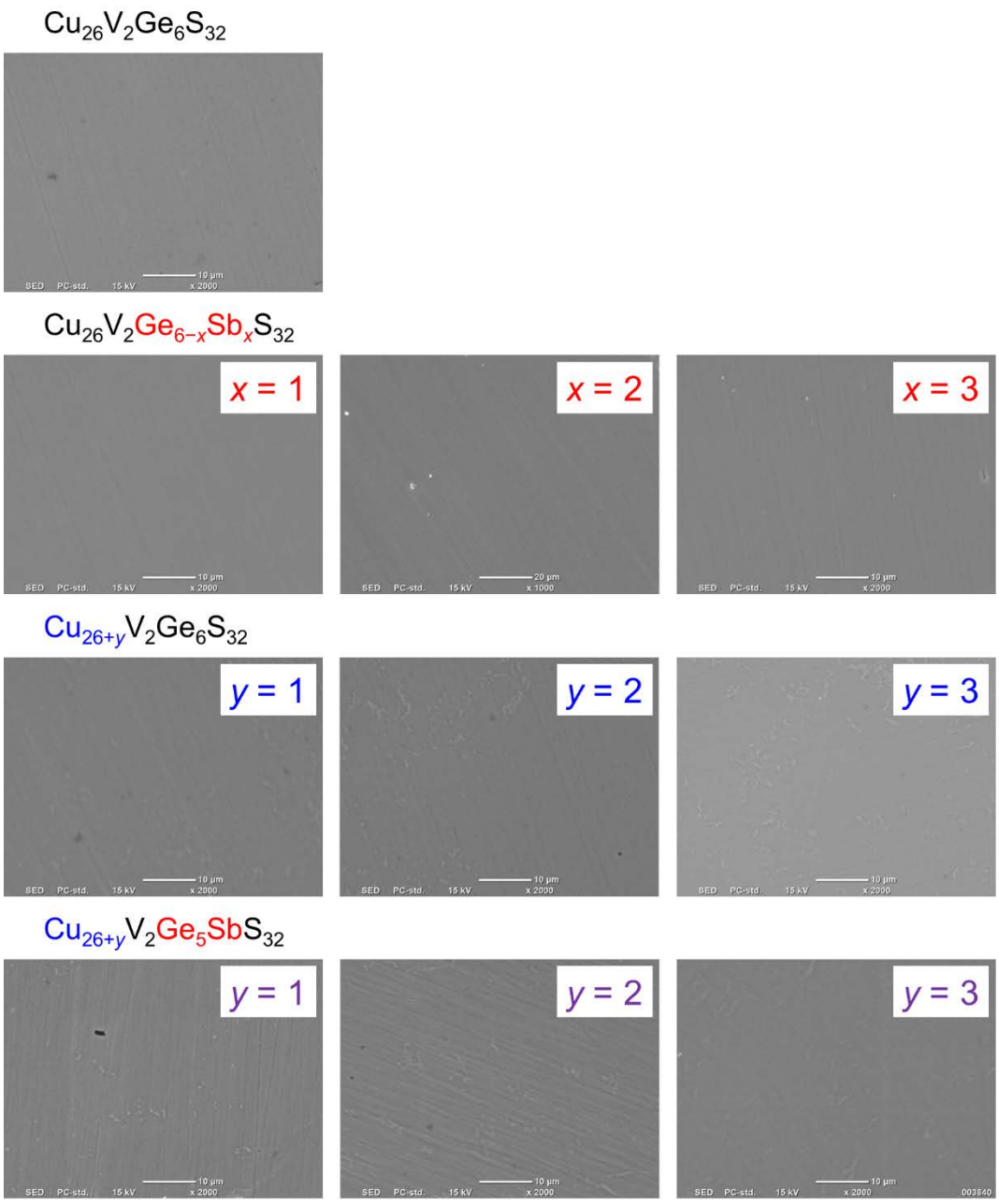

Figure S14. Scanning electron microscopy images for $Cu_{26}V_2Ge_{6-x}Sb_xS_{32}$, $Cu_{26+y}V_2Ge_6S_{32}$, and $Cu_{26+y}V_2Ge_{6-x}Sb_xS_{32}$ (x = 1) samples.

Table S3. Hole carrier concentration n and Hall mobility μ_H for $Cu_{26}V_2Ge_{6-x}Sb_xS_{32}$, $Cu_{26+y}V_2Ge_6S_{32}$, and $Cu_{26+y}V_2Ge_{6-x}Sb_xS_{32}$ (x = 1) samples.

	n / 10^{21} m^{-3}	μ_H / cm^2 V^{-1} s^{-1}
$x = y = 0$	6.8	5.5
$x = 1, y = 0$	5.5	4.0
$x = 2, y = 0$	4.0	2.8
$x = 3, y = 0$	1.9	1.9
$x = 0, y = 2$	5.1	2.6
$x = 0, y = 3$	4.1	1.6
$x = 1, y = 3$	1.7	1.0

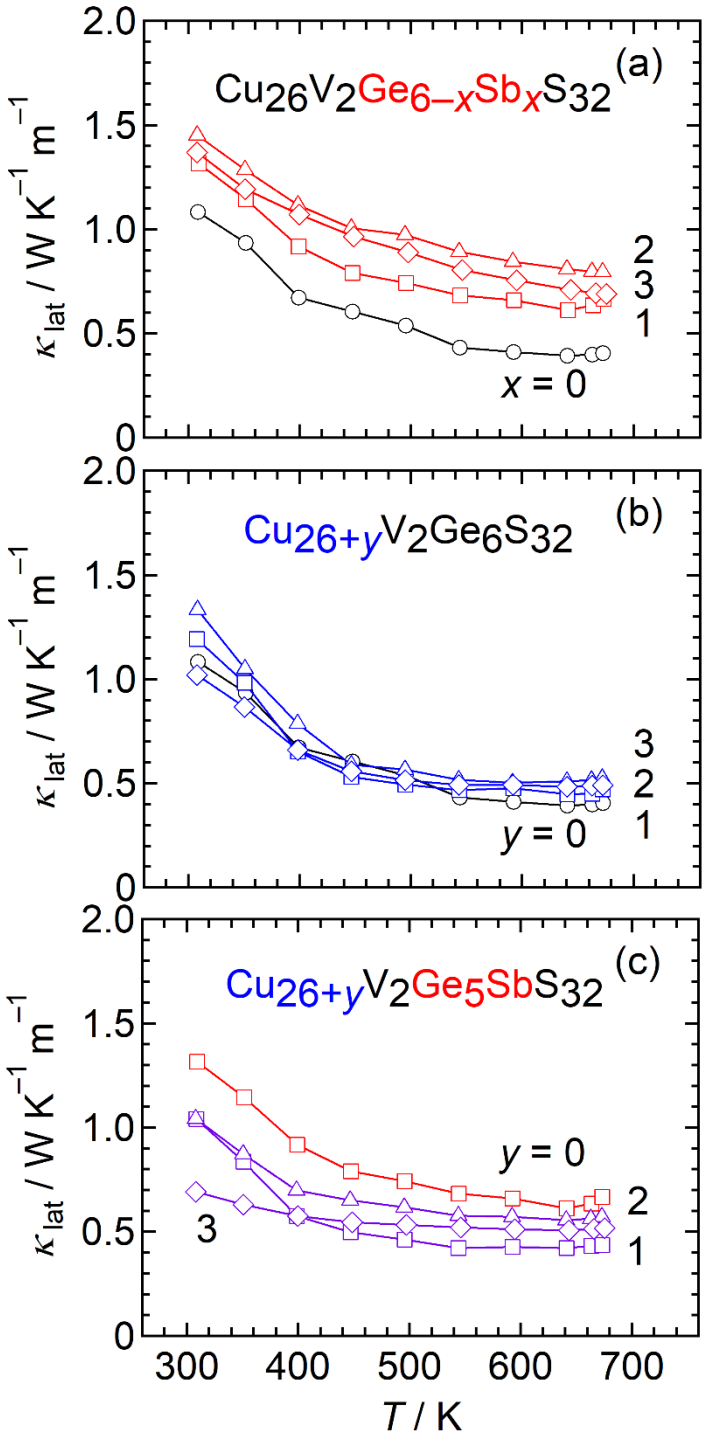

Figure S15. Lattice thermal conductivity κ_{lat} for $Cu_{26}V_2Ge_{6-x}Sb_xS_{32}$, $Cu_{26+y}V_2Ge_6S_{32}$, and $Cu_{26+y}V_2Ge_{6-x}Sb_xS_{32}$ (x = 1) samples.

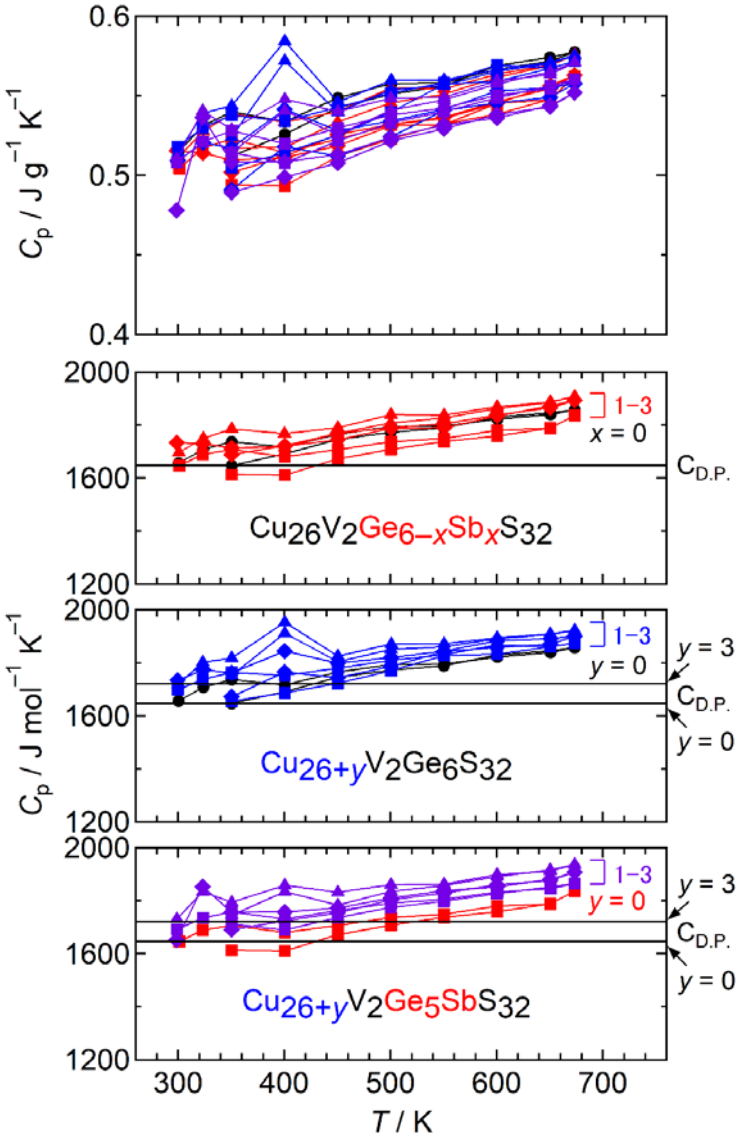

Figure S16. Specific heat C_p in units of J g^{-1} K^{-1} and J mol^{-1} K^{-1} for $Cu_{26}V_2Ge_{6-x}Sb_xS_{32}$, $Cu_{26+y}V_2Ge_6S_{32}$, and $Cu_{26+y}V_2Ge_{6-x}Sb_xS_{32}$ (x = 1) samples.